analytical chemistry

pubs.acs.org/ac Article

CRISPR-Cas12a-Derived Photoelectrochemical Biosensor for Point-Of-Care Diagnosis of Nucleic Acid

Ruijin Zeng,[§] Hexiang Gong,[§] Yanli Li, Yuxuan Li, Wei Lin, Dianping Tang,* and Dietmar Knopp*

Cite This: *Anal. Chem.* 2022, 94, 7442−7448 Read Online

ACCESS | Metrics & More | Article Recommendations | Supporting Information

ABSTRACT: This work presented a point-of-care (POC) photoelectrochemical (PEC) biosensing for the detection of human papillomavirus-16 (HPV-16) on a portable electrochemical detection system by using CRISPR-Cas12a trans-cleaving the G-quadruplex for the biorecognition/amplification and a hollow In_2O_3−In_2S_3-modified screen-printed electrode (In_2O_3−In_2S_3/SPE) as the photoactive material. G-quadruplexes were capable of biocatalytic precipitation (H_2O_2-mediated 4-chloro-1-naphthol oxidation) on the In_2O_3−In_2S_3/SPE surface, resulting in a weakened photocurrent, but suffered from trans-cleavage when the CRISPR-Cas12a system specifically recognized the analyte. The photocurrent results could be directly observed with the card-sized electrochemical device *via* a smartphone, which displayed a high-value photocurrent for these positive samples, while a low-value photocurrent for the target-free samples. Such a system exhibited satisfying photocurrent responses toward HPV-16 within a wide working range from 5.0 to 5000 pM and allowed for detection of HPV-16 at a concentration as low as 1.2 pM. The proposed assay provided a smartphone signal readout to enable the rapid screening PEC determination of HPV-16 concentration without sophisticated instruments, thus meeting the requirements of remote areas and resource-limited settings. We envision that combining an efficient biometric PEC sensing platform with a wireless card-sized electrochemical device will enable high-throughput POC diagnostic analysis.

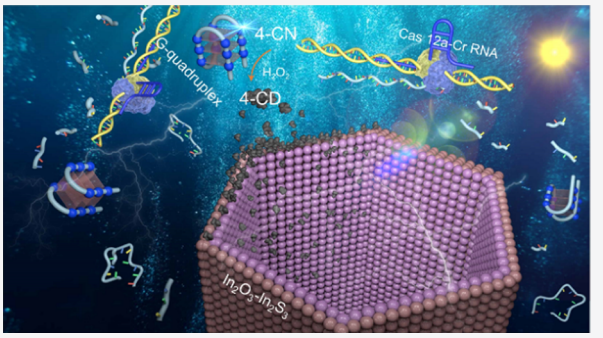

Photoelectrochemical (PEC) bioanalysis has been attracting increasing attention as the generation of the PEC photocurrent resulting from the biointeractions (aptamer binding and immunoaffinity) on photoactive-material-rendered PEC biosensor with unique technique superiority (*e.g.*, high sensitivity, quick response, and diverse signal-transducing mechanisms).[1−4] Despite many advances in this field, two significant issues have been restricting the development of PEC biosensors. Specifically, to obtain more stable photocurrent readings, binary or even multielement heterojunctions are usually used as the photoactive substrates for the biosensing applications.[5−7] The multicomponent composites can achieve a higher and more stable photocurrent readout than the single photocatalytic materials; however, our previous work found that the composites only improved the background photocurrent value but not necessarily increased the sensitivity to the analyte-triggered product. In this case, the "signal-off" mode is also chosen to construct a series of PEC sensors for highly sensitive bioanalysis. Diverse schemes involving analyte-induced ion exchange or construction of heterojunctions have been reported in the field of PEC bioanalysis to reduce the background photocurrent for the quantitative detection of analytes.[8−10] However, such "signal-off" modes often suffer from disturbances because of the unavoidable photocorrosion phenomena. In this regard, it is imperative to rationally construct advanced signal transduction models capable of combining composite materials and "signal-on" models for sensitive detection purposes. Moreover, the existing detection methods are mainly focused on expensive large-scale electrochemical workstations and complex analysis procedures, which further limits the development of PEC biosensors toward low-cost and portability analysis to a certain extent.[11−13] In recent years, smartphones, as portable mobile devices, have played an increasingly important role in biomedical analysis, rapid disease diagnosis, food safety assessment, and environmental monitoring due to their advantages of touch screens, wireless transmission, and programmable systems.[14−18] Meanwhile, with the development of integrated circuit technology, many highly integrated and miniaturized devices with cloud-based data have been constructed to replace sophisticated analytical instruments and equipment to complete the detection and reading of signals. Therefore, the combination of smartphones and integrated circuits to replace traditional electrochemical

Received: March 29, 2022
Accepted: April 29, 2022
Published: May 12, 2022

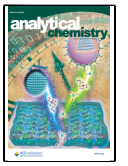

https://doi.org/10.1021/acs.analchem.2c01373
Anal. Chem. 2022, 94, 7442−7448

Scheme 1. Schematic Illustration of POC PEC Biosensing for the Detection of Human Papillomavirus-16 (HPV-16) Coupled with CRISPR-Cas12a trans-cleaving the G-Quadruplex/Hemin for the Catalysis of 4-Chloro-1-naphthol (4-CN) to Benzo-4-Chloro-Hexadienone (4-CD) Precipitates in the Presence of H_2O_2 for the Biosignal Recognition/Amplification and Hollow In_2O_3−In_2S_3 Photoactive Materials

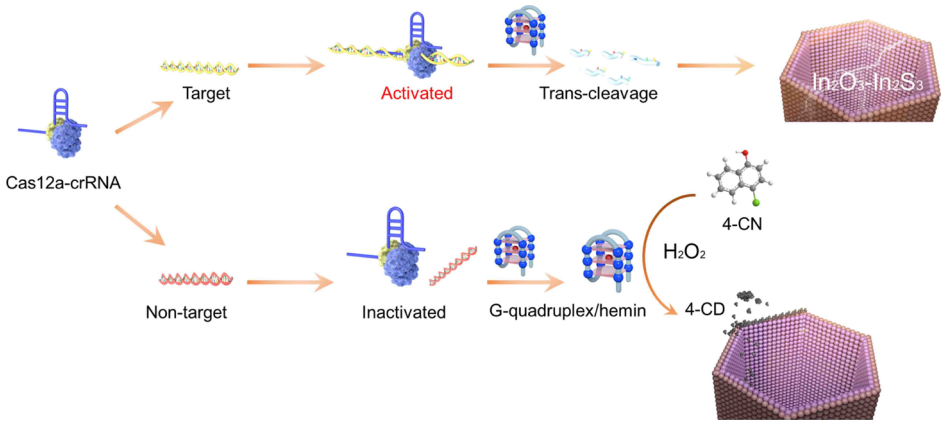

workstations to build a portable platform is of great significance for expanding the application of PEC biosensing.

Clustered regularly interspaced short palindromic repeats (CRISPR)/CRISPR-associated (Cas) proteins systems are gradually employed as a novel diagnostic toolkit for ultrasensitive nucleic acid detection by using the "collateral cleavage" activity (nonspecific nucleic acid-cutting activities).[19−21] In the past two years, our group has also constructed a series of biosensors to detect nucleic acids by using Cas12a's collateral cleavage ability to digest ssDNA. For instance, Zeng *et al.* devised a CRISPR-Cas12a-mediated instrument-free piezoresistive biosensor for the detection of human papillomavirus by using an MXene-PEDOT:PSS film as piezoresistive material.[22] Gong *et al.* established a sensing system for the ultrasensitive PEC bioassay based on dopamine-loaded liposome-encoded magnetic beads cleaved by CRISPR-Cas12a.[23] More interestingly, Li and colleagues were surprised to find that the activated Cas12a protein also has a good trans-cleaveing activity on the DNA G-quadruplexes.[24] We speculate that the ability of G-quadruplex DNAzyme to oxidize 4-chloro-1-naphthol (4-CN) to generate insoluble precipitates may be deprived after the cleavage.

As a typical n-type semiconductor with a narrow bandgap of about 2.8 eV, In_2O_3 is widely used in photocatalytic applications due to its excellent stability and low toxicity. The hollow In_2O_3 nanotubes obtained by high-temperature calcination of MIL-68(In) have a large specific surface area and a good mass transfer ability. More importantly, In_2O_3 can easily form heterojunctions with other semiconductors by chemical growth to enhance the photocurrent response. Among various semiconductors, In_2S_3 and In_2O_3 can be synthesized by simple ion exchange and have a good photocurrent response due to a suitable energy band matching. Herein, we report a novel "signal-on" PEC biosensing based on the exquisite integration of hollow In_2O_3−In_2S_3 with the versatile function of CRISPR-Cas12a trans-cleaving the G-quadruplex configuration (Scheme 1). This method utilizes Cas12a-CrRNA to identify target nucleic acid fragments for conversion to indiscriminately trimmed G-quadruplexes. The G-quadruplex/hemin complex has a peroxidase-like activity, which can catalyze 4-CN to form a benzo-4-chloro-hexadienone (4-CD) precipitate on the In_2O_3−In_2S_3/SPE surface, resulting in a decreased photocurrent. The photocurrent signal recovered when G-quadruplex was cleaved by activated Cas12a-CrRNA, which was positively correlated with the analyte concentration. To enhance the portability of the PEC sensing, we integrate the signal converter and signal readout into the miniaturized portable device and smartphones with low-cost and easy-to-operate, which may provide a promising method for the sensitive and disposable point-of-care (POC) detection for molecular diagnostics.

EXPERIMENTAL SECTION

Preparation of MIL-68(In)-Derived In_2O_3−In_2S_3. The In_2O_3 powder was synthesized by thermal annealing of hexagonal MIL-68(In) precursors. In brief, $In(NO_3)_3{\cdot}xH_2O$ (1.8 mmol) and 1, 4-benzenedicarboxylic acid (1.8 mmol) were mixed in DMF (15 mL, containing 80 mL of a 40 mmol/L NaOAc solution) with continuous stirring. Thereafter, the above solution was placed in an oil bath at 100 °C for 0.5 h (operate in a fume hood). After the vessel was removed from the oil bath and cooled to room temperature, the white precipitate (MIL-68(In)) was washed several times with deionized water and ethanol. The MIL-68(In) (0.5 g) was placed in a crucible and kept at 500 °C for 60 min at a heating rate of 2 °C/min and then cooled down to obtain light yellow In_2O_3. In_2O_3−In_2S_3 thin films were grown on an amorphous glass substrate *via* the simple successive ionic layer adsorption and reaction (SILAR) method. The In_2O_3-loaded glass plate was obtained by dispersing 10 mg of In_2O_3 material on the surface of the glass plate and drying. The In_2O_3-loaded glass plate was immersed in a Na_2S solution (0.1 mol/L, 20 mL) for 1 min, then removed, rinsed gently with distilled water, and placed in an $InCl_3$ solution (0.1 mol/L, 20 mL) for 1 min. The above operation was repeated six times to get In_2O_3−In_2S_3.

Fabrication of the CRISPR-Cas12a-Driven Portable PEC Platform and Measurement. Prior to the experiment, the In_2O_3−In_2S_3 solution (5.0 mL, 1.0 mg/mL) was dripped onto screen-printed electrodes and dried to obtain In_2O_3−In_2S_3/SPE. Briefly, nonactivated Cas12a were preassembled by incubating Cas12a (100 nM, 40 μL) with crRNA (120 nM, 40 μL) at 37 °C for 30 min. Subsequently, a reaction buffer (80 μL) containing the different concentration targets (8 μL; annealed at 95 °C beforehand), Cas12a-CrRNA (40 nM, 20 μL), G4 DNA sequence (25 μL, 500 nM containing 200 nM hemin and 10 mM KCl) and nuclease-free water were

https://doi.org/10.1021/acs.analchem.2c01373
Anal. Chem. 2022, 94, 7442−7448

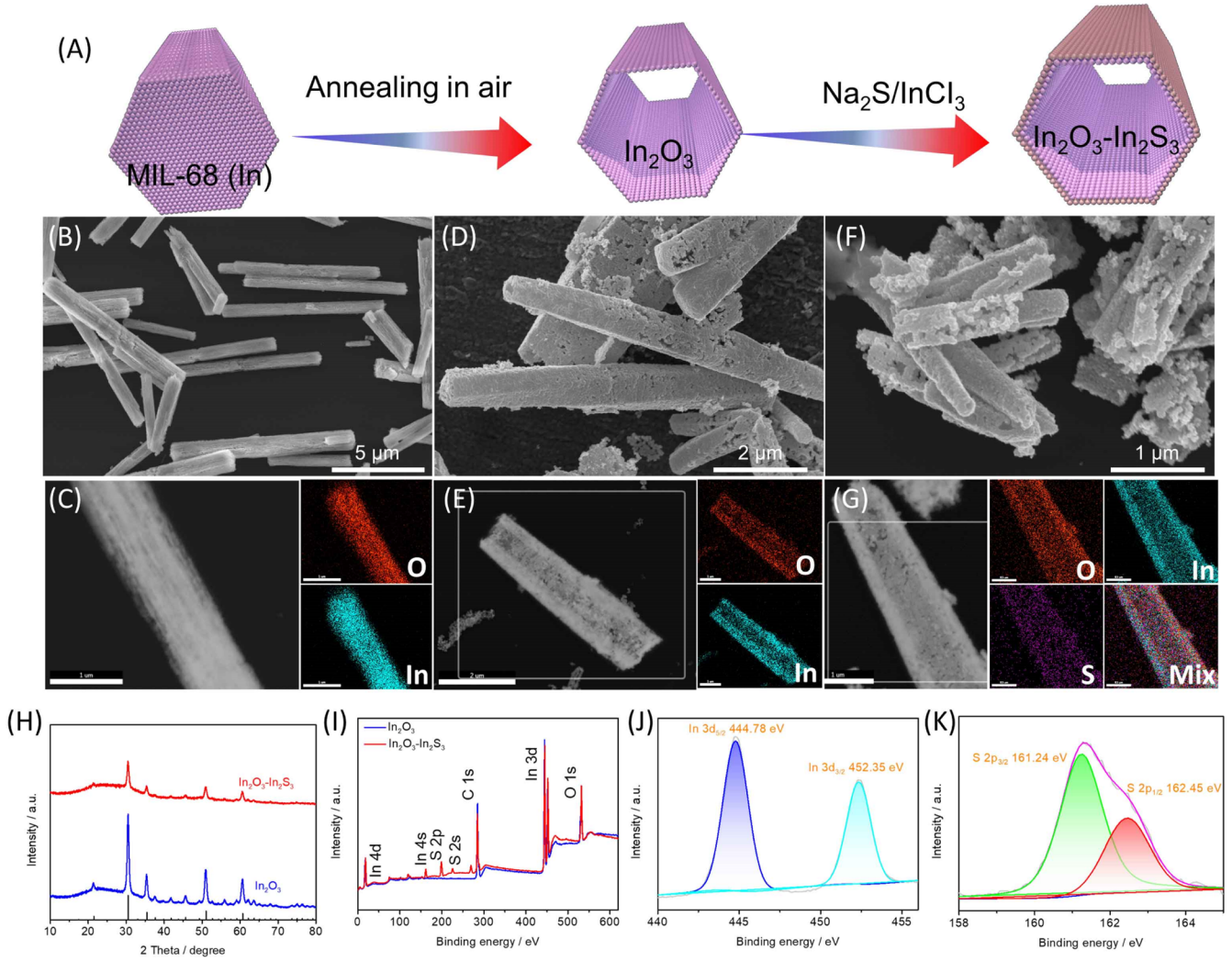

Figure 1. (A) Schematic illustration of the synthetic process of In_2O_3−In_2S_3; SEM images of (B) MIL-68(In), (D) In_2O_3, and (F) In_2O_3−In_2S_3; element mapping of (C) MIL-68(In), (E) In_2O_3, and (G) In_2O_3−In_2S_3; (H) XRD patterns and (I) XPS survey spectra of In_2O_3 and In_2O_3−In_2S_3; high-resolution XPS spectra of (J) In 3d and (K) S 2p.

incubated at 37 °C for 60 min. Next, 4-CN (1.5 mg/mL, 25 μL) and H_2O_2 (10 mM, 5 μL) were added into the above solution and maintained for 30 min to generate 4-CD. Afterward, the reacted solution was dropped on the In_2O_3−In_2S_3/SPE surface and air-dried at room temperature. Finally, the as-prepared In_2O_3−In_2S_3/SPE was used as a photoelectrode for PEC detection in an Na_2SO_4- (0.1 mol/L, containing 10 mmol/L ascorbic acid) supporting electrolyte. The smartphone acts as a display terminal and control center to obtain the measured photocurrent graphs for further analysis.

RESULTS AND DISCUSSION

Characterization of MIL-68(In), In_2O_3, and In_2O_3−In_2S_3. Figure 1A shows a brief schematic diagram of the synthesis process of the In_2O_3−In_2S_3 hollow nanostructures. Well-defined MIL-68(In) rods are synthesized by a simple oil bath method in the DMF solvent of indium(III) nitrate hydrate and 1,4-benzenedicarboxylic acid with sodium acetate as the modulator. The formation of the In_2O_3 hollow nanotubes occurred by high-temperature calcination of MIL-68(In) hexagonal rods. Finally, the In_2S_3 nanoparticles were supported on In_2O_3 to form In_2O_3−In_2S_3 nanotubes through the SILAR method at room temperature. The specific morphology and corresponding transformation processes of the resulting samples [MIL-68(In), In_2O_3, and In_2O_3−In_2S_3] were characterized by scanning electron microscopy (SEM). SEM images in Figure 1B revealed MIL-68(In) at a micron-scale with a regular solid rod-like structure. The corresponding elemental mapping (Figure 1C) demonstrates the coexistence of In and O elements throughout the composite. After annealing the MIL-68(In) precursor to In_2O_3 at high temperature, size reduction and a large number of voids and cracks on the surface were observed (Figure 1D). The shrinkage of the precursor framework and the formation of the porous structure may be attributed to the decomposition of the organic ligands of terephthalic acid. At the same time, the corresponding element mapping (Figure 1E) and energy dispersive spectrometer (EDS) spectrum (Figure S1) showed the coexistence of In and O elements, accompanied by an obvious hollow morphology. SEM images of SILAR-treated In_2O_3 nanotubes showed more aggregation and formation of nanoparticles on the surface (Figure 1F). Elemental mapping and EDS showed that In, O, and S elements were present in the nanostructure, indicating the successful incorporation of the S element and the formation of In_2S_3 (Figures 1G and S2).

https://doi.org/10.1021/acs.analchem.2c01373
Anal. Chem. 2022, 94, 7442−7448

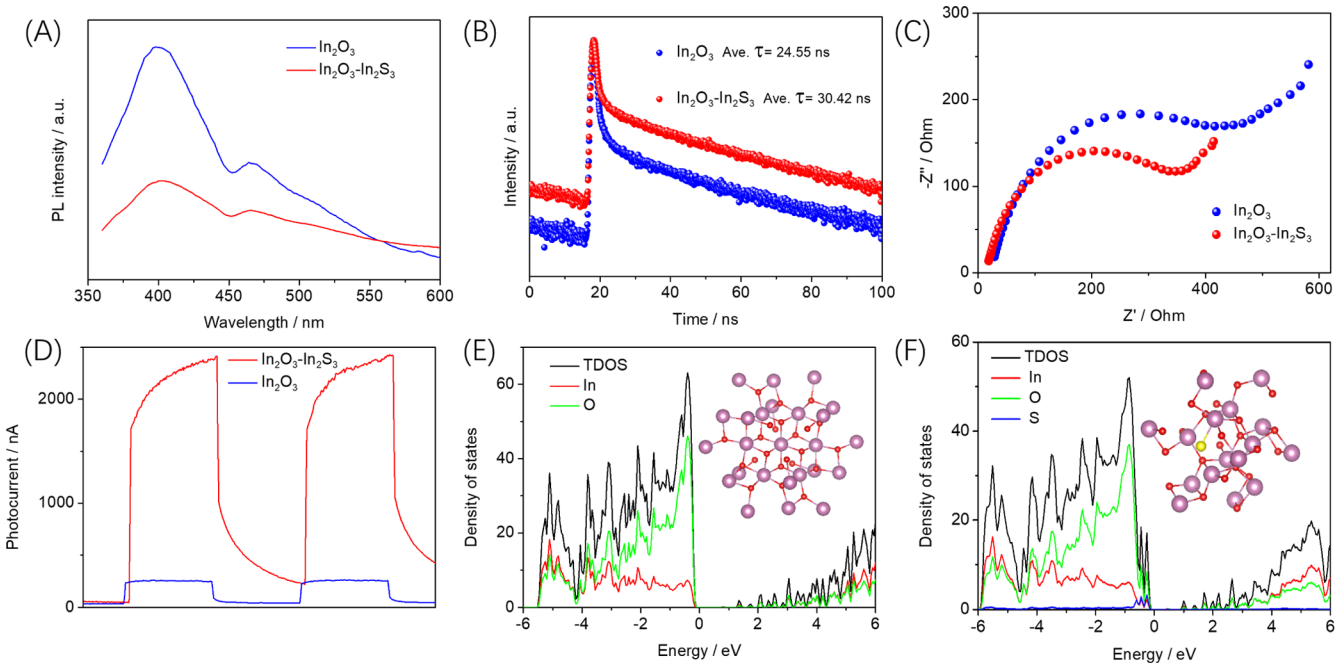

Figure 2. (A) Steady-state PL spectra, (B)TRPL decay, (C) EIS Nyquist plots, and (D) periodic on/off photocurrent responses of In_2O_3 and In_2O_3−In_2S_3; calculated DOS and corresponding optimized structural model (inset) of (E) In_2O_3 and (F) In_2O_3−S_1.

Besides, the crystal structure and surface chemical valence state in the preparation of the above materials were further analyzed. The MIL-68(In) displayed several primary diffraction peaks in X-ray diffraction (XRD) at 8.06, 9.30, 14.02, 16.24, 16.88, 18.74, 26.30, 29.70, and 31.12°, which are consistent with the previous literature reports (Figure S3).[2] The In_2O_3 powder derived from calcining MIL-68(In) in air displayed five diffraction peaks at 21.36, 30.50, 35.36, 51.00, and 60.62°, which matched well with the (211), (222), (400), (440), and (622) crystal planes of the cubic structure In_2O_3, respectively (JCPDS no. 06-0416; Figure 1H). The XRD peak patterns of In_2O_3−In_2S_3 obtained by the SILAR treatment are almost identical to those of In_2O_3, which may be attributed to the smaller amount of In_2S_3 loading. As shown from the X-ray photoelectron spectroscopy (XPS) survey spectrum in Figure 1I, besides the valence states of In (4d, 4s, and 3d) and O (1s) elements, the formation of new S (2s and 2p) valence states were introduced after SILAR-treatment, which is consistent with the results of elemental mapping. The high-resolution In 3d spectrum of In_2O_3−In_2S_3 shows twin peaks with binding energies of 444.78 and 452.35 eV, corresponding to characteristic spin−orbit split In $3d_{5/2}$ and In $3d_{3/2}$ of trivalent indium, respectively (Figure 1J).[25] Besides, the S 2p spectrum can be deconvoluted into two major peaks located at 161.24 eV (S $2p_{3/2}$) and 162.45 eV (S $2p_{1/2}$), respectively, which are ascribed to S−In coordinated with the state of S^{2-} (Figure 1K).[26]

Charge Carrier Behaviors and the DFT Calculation of In_2O_3 and In_2O_3−In_2S_3. Since the intensity of the photocurrent is the key to the signal readout and quantitative detection of the whole sensor, the optical/photoelectrochemical properties of In_2O_3 before and after loading In_2S_3 were characterized. The optical absorption performance of In_2O_3 and In_2O_3−In_2S_3 samples was characterized by UV−vis diffuse reflectance spectroscopy (DRS, Figure S4). The pale yellow In_2O_3 has an intrinsic absorption in the range of 200−460 nm and a weak absorption in the range of 460−800 nm, indicating that the absorption range is mainly in the UV area. After the In_2S_3 modification, the absorption edges of In_2O_3−In_2S_3 moved toward the visible-light region (redshifted to around 520 nm), suggesting that the formation of In_2S_3 on the surface of In_2O_3 can effectively improve the light absorption properties of In_2O_3. Meanwhile, the charge carrier dynamics and the lifetimes of In_2O_3 before and after loading In_2S_3 were further investigated by photoluminescence (PL, photoexcitation wavelength set at 350 nm) and time-resolved PL (TRPL). The steady-state PL spectral emission peak intensity of In_2O_3−In_2S_3 is remarkably lower compared to that of pristine In_2O_3, indicating that the formation of In_2O_3−In_2S_3 helps to suppress the photoinduced carrier recombination (Figure 2A). Meanwhile, the TRPL decay spectra and the corresponding biexponential fitting results show that the average lifetime of In_2O_3−In_2S_3 (τ = 30.42 ns) is longer than that of In_2O_3 (τ = 24.55 ns), illustrating the possible existence of an efficient interfacial electron transfer between In_2O_3 and In_2S_3 (Figure 2B). Moreover, electrochemical impedance spectra (EIS; Figure 2C) and the transient photocurrent response measurement (Figure 2D) showed that In_2O_3−In_2S_3 had a smaller semicircle in Nyquist plots and a stronger photocurrent intensity than In_2O_3. These optical/photoelectrochemical tests results above collectively demonstrate the better light absorption properties and an increased separation and transfer of photoexcited carriers in In_2O_3−In_2S_3.

To help elucidate the effect of the SILAR treatment on the photocurrent enhancement of In_2O_3, a first-principles density functional theory (DFT) approach was performed. The calculated density of states (DOS) of In_2O_3 reveals typical semiconductor characteristics with a narrow bandgap of 1.30 eV (Figure 2E). The resulting bandgap is smaller than the experimental value due to DFT limitations, but it is reasonable to use the same exchange and correlation functions to calculate the relative value of the bandgap. We then replaced one O with S in In_2O_3 to observe the effect of introducing the S element on DOS. As shown in Figure 2F, O and S elements contributed

https://doi.org/10.1021/acs.analchem.2c01373
Anal. Chem. 2022, 94, 7442−7448

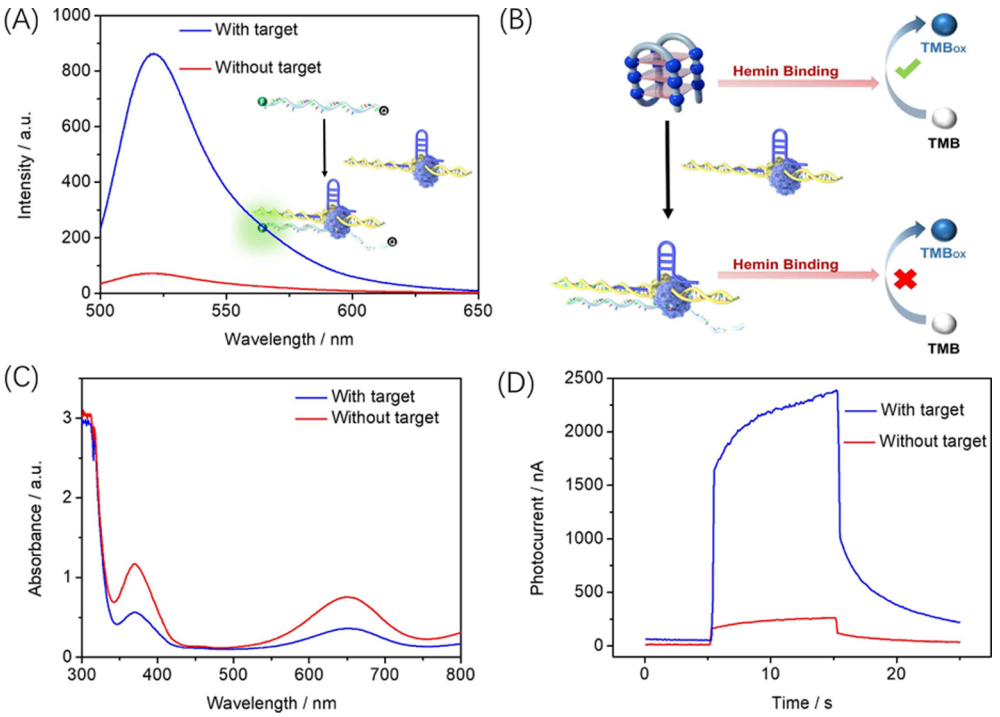

Figure 3. (A) Fluorescence responses of Cas12a + CrRNA + FQ-ssDNA with or without HPV-16; (B) schematic illustration of target-activated CRISPR-Cas12a trans-cleaveage of G-quadruplexes. The cleavage of DNA G-quadruplexes was verified with the TMB-H_2O_2 system; (C) UV−vis absorption spectra of Cas12a + CrRNA + G-quadruplexes + hemin + TMB (2 mM) + H_2O_2 (0.5 mM) with or without HPV-16; (D) photoelectrochemical responses of Cas12a + CrRNA + G-quadruplexes + hemin + H_2O_2 + 4-CN with or without HPV-16.

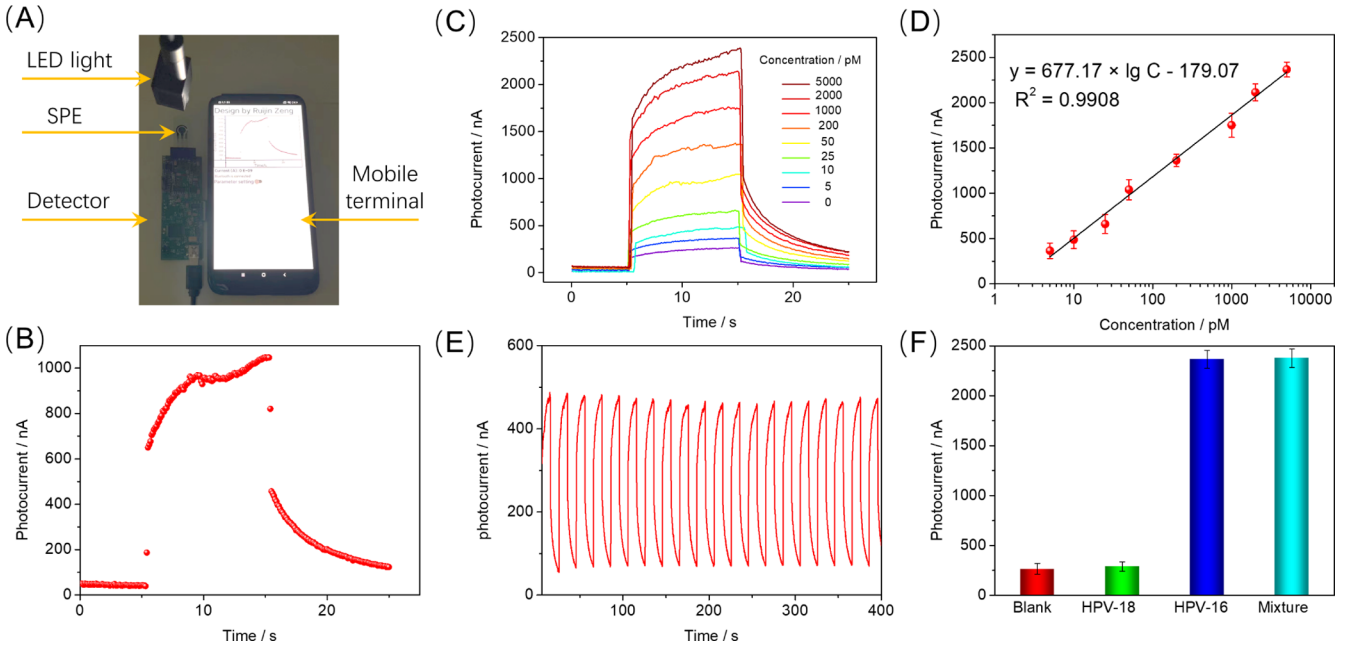

Figure 4. (A) Photograph of a smartphone-based portable PEC biosensor (main components are LED lights, integrated circuit boards, and smartphone terminals); (B) plotted with data obtained from the smartphone in (A); (C) photocurrent−time curves of In_2O_3−In_2S_3/SPE toward HPV-16 with different concentrations (0, 5.0, 10, 25, 50, 200, 1000, 2000, and 5000 pM); (D) corresponding calibration curve between the peak photocurrent and HPV-16 concentrations; € photocurrent−time curves under an on/off irradiation cycle for 20 times (within 400 s); (F) specificity of the CRISPR-Cas12a-based portable PEC biosensor for 5000 pM of HPV-16 by comparing with the high-risk type (HPV-18) added at a 10 nM level.

new peaks near the valence band maximum, resulting in a smaller bandgap of 0.95 eV. An increase in DOS at the valence band maximum and a decrease in the bandgap are observed in In_2O_3−S_1, implying that electrons are easily thermally excited into the conduction band under light irradiation, leading to a higher photoconversion efficiency in In_2O_3−S_1.[27]

Verification of the Feasibility. We then needed to further verify whether the analyte could activate the CRISPR-Cas12a

https://doi.org/10.1021/acs.analchem.2c01373
Anal. Chem. 2022, 94, 7442−7448

system and cleave the G-quadruplex. For validation, fluorophore (F) and quencher (Q)-labeled short ssDNA fluorophores were used as reporter substrates. HPV-16 is recognized by Cas12a-CrRNA to form a Cas12a-CrRNA-HPV-16 ternary complex, which then activates the cleavage of the reporter substrate by Cas12a, resulting in the recovery of the fluorescent signal. As shown in Figure 3A, Cas12a-CrRNA-HPV-16 was able to restore the fluorescence of the reporter substrate compared to HPV-16-free samples, indicating that HPV-16 could activate the cleavage ability of Cas12a. Next, we replaced the reporter substrate with a G-quadruplex to verify the G-quadruplex cleavage ability of Cas12a-crRNA-HPV-16 and used the TMB-H_2O_2 system to analyze the cleavage of the G-quadruplex (Figure 3B).

As expected, the TMB-H_2O_2 system absorbance intensity decreased in the presence of HPV-16, suggesting that active Cas12a would indiscriminately cleave surrounding G-rich sequences and prevent the formation of G-quadruplex structures, further inhibiting the peroxide enzyme-like activity (Figure 3C). Furthermore, the polyacrylamide gel electrophoresis (PAGE) results showed that the G-quadruplex was degraded to some extent in the presence of the analyte compared to lane "a" and lane "b" (Figure S5). Finally, we replaced TMB with 4-CN to verify the effect of Cas12a-crRNA-HPV-16 on the ability of the G-quadruplex to catalyze insoluble precipitation on In_2O_3−In_2S_3/SPE. A lower photocurrent response was obtained in the absence of HPV-16, which is mainly that the G-quadruplex/hemin can accelerate the biocatalytic precipitation of 4-CN on the surface of In_2O_3−In_2S_3/SPE *via* H_2O_2 (Figure 3D, red line). The activation of Cas 12a in the presence of HPV-16 cleaves the G-quadruplex, blocks the biocatalytic precipitation process, and obtains a strong photocurrent response (Figure 3D, blue line). Based on the above results, we might conclude that the In_2O_3−In_2S_3/SPE-based PEC sensing platform could be preliminarily applied for monitoring of HPV-16 by coupling with the CRISPR-Cas12a system and the G-quadruplex/hemin-based biocatalytic precipitation method.

Analytical Performance of the Portable PEC Biosensor. To make the whole biosensor more portable and simpler, we designed a detection system including a LED light, a self-designed electronic circuit, and a signal recording smartphone. In simple terms, the electronic circuit converts the obtained PEC photocurrent into a digital signal through an analog-to-digital converter and transmits it to a smartphone using a Bluetooth module. Figure 4A is a photograph of PEC detection using a portable device. The data obtained from the smartphone can be further analyzed and graphed (Figure 4B). The as-prepared PEC portable biosensor was adopted for the detection of HPV-16 standards with the different concentrations (0−5000 pM) by coupling with CRISPR-Cas12a trans-cleaving the G-quadruplex strategy and hollow In_2O_3−In_2S_3/SPE. As the HPV-16 concentration increased, more G-quadruplex/hemin was cleaved and could not catalyze 4-CN to produce insoluble precipitates, resulting in an increase in the photocurrent of the In_2O_3−In_2S_3/SPE. A preferable linear correlation between the response photocurrent and the HPV-16 concentration was acquired (Figure 4C). The regression equation was expressed as I (nA) = 677.17 × log $C_{[HPV\text{-}16]}$ − 179.07 (pM) (R^2 = 0.9908, n = 8) with a limit of detection (LOD) of 1.3 pM (S/N = 3) (Figure 4D). More importantly, compared with other CRISPR-Cas12a-based strategies to detect HPV-16 (Table S1), this method enables a lower LOD and more portable detection technology and readout. Besides, the maximum relative standard deviations (RSDs, n = 3) were 5.77 % for intra-assays, and 8.34 % for interassays toward 10, 200, and 5000 pM HPV-16, respectively, indicating good reproducibility. Moreover, the photocurrent of In_2O_3−In_2S_3/SPE did not change significantly within 400 s of illumination, indicating that the In_2O_3−In_2S_3/SPE has an excellent photostability and photocorrosion resistance (Figure 4E). The selectivity of the portable PEC biosensor was then examined using another high-risk HPV genotype (HPV-18) as an interfering substance. In the presence of 10 nM HPV-18, the photocurrent of In_2O_3−In_2S_3/SPE was similar to that of the blank sample. Furthermore, in the presence of 5000 pM HPV-16 and 10 nM HPV-18, the photocurrent values were similar to those in the presence of 5000 pM HPV-16 alone, indicating the excellent anti-interference ability of the PEC portable biosensor (Figure 4F). The unrecognized response of HPV-18 can be attributed to the good specific recognition ability of the CRISPR-Cas12a system.

Analysis of Real Samples. To investigate the method accuracy and interlaboratory validation of our system, we collected 4 clinical cervical brush samples from Fujian Provincial Hospital (Fuzhou, China) according to the rules and the local ethical committee (note: informed consents were obtained from human participants of this study). Prior to measurement, these samples were initially centrifuged for 5 min at 5000g to remove the possible precipitates and then were determined using our system and PCR fluorescent assay as a reference method (note: PCR fluorescent assays were carried out with Clinical Laboratory and Medical Diagnostics Laboratory of Fujian Provincial Hospital, China). All data obtained from these two methods are shown in Table 1. The

Table 1. Comparison of the Results Obtained From the PEC Biosensor and the Commercial PCR Fluorescent Method for Human Cervical Samples

	method; conc. (mean ± SD, n = 3, pM)		
sample no.	PEC biosensor	PCR method	t_{exp}
1	55.69 ± 3.32	52.36 ± 2.96	1.06
2	22.77 ± 1.94	23.15 ± 1.39	0.93
3	96.61 ± 6.51	95.44 ± 5.32	0.61
4	83.11 ± 6.39	81.42 ± 7.03	1.39

statistical analysis of the experimental results was executed using a t-test method. No significant differences at the 0.05 significance level were encountered in the analysis of the 4 clinical samples between the two methods because all t_{exp} values were below 2.77 ($t_{crit[0.05,4]}$ = 2.77). To further highlight the advantages of our method, 3 HPV standards, including 5.0, 50, and 100 pM, were spiked into blank human serum samples using standard addition methods for recovery studies. As shown in Table S2, the recoveries ranged from 97.23 to 102.36%, declaring an acceptable accuracy for the quantitative analysis of the target in the clinical sample.

CONCLUSIONS

In short, this contribution successfully devised portable PEC biosensing for the quantitative determination of human papillomavirus-16 (HPV-16) by coupling CRISPR-Cas12a trans-cleavage of the G-quadruplex with a hollow In_2O_3−In_2S_3-modified electrode system. The delicate integration of the CRISPR-Cas12a system and G-quadruplex-catalyzed

https://doi.org/10.1021/acs.analchem.2c01373
Anal. Chem. 2022, 94, 7442−7448

precipitation allowed In_2O_3–In_2S_3/SPE to exhibit a low background photocurrent signal in the absence of the analyte. In the presence of the analyte, the photocurrent of the In_2O_3–In_2S_3/SPE is increased due to the cleavage of the G-quadruplex by Cas12a-CrRNA, realizing the "signal-on" mode. In addition, the self-designed circuit module and smartphone APP could make the entire PEC inspection process simpler and get rid of the use of traditional large-scale instruments. We envision that PEC biosensing systems and portable devices with strong specific recognition capabilities represent a significant step toward developing a more portable and low-cost strategy in clinical and environmental monitoring.

■ ASSOCIATED CONTENT

Supporting Information

The Supporting Information is available free of charge at https://pubs.acs.org/doi/10.1021/acs.analchem.2c01373.

Materials and reagents, theoretical calculation method, EDS spectrum of In_2O_3, EDS spectrum of In_2O_3–In_2S_3, XRD patterns of MIL-68(In), UV–vis DRS of In_2O_3 and In_2O_3–In_2S_3, and PAGE results (PDF)

■ AUTHOR INFORMATION

Corresponding Authors

Dianping Tang − *Key Laboratory of Analytical Science for Food Safety and Biology (MOE & Fujian Province), Department of Chemistry, Fuzhou University, Fuzhou 350108, People's Republic of China;* orcid.org/0000-0002-0134-3983; Phone: +86-591-2286 6125; Email: dianping.tang@fzu.edu.cn; Fax: +86-591-2286 6135

Dietmar Knopp − *Department of Chemistry, Chair for Analytical Chemistry and Water Chemistry, Institute of Hydrochemistry, Technische Universität München, Garching D-85748, Germany;* orcid.org/0000-0003-4566-9798; Phone: +49-89-289 54500; Email: dietmar.knopp@mytum.de

Authors

Ruijin Zeng − *Key Laboratory of Analytical Science for Food Safety and Biology (MOE & Fujian Province), Department of Chemistry, Fuzhou University, Fuzhou 350108, People's Republic of China*

Hexiang Gong − *Key Laboratory of Analytical Science for Food Safety and Biology (MOE & Fujian Province), Department of Chemistry, Fuzhou University, Fuzhou 350108, People's Republic of China*

Yanli Li − *Key Laboratory of Analytical Science for Food Safety and Biology (MOE & Fujian Province), Department of Chemistry, Fuzhou University, Fuzhou 350108, People's Republic of China*

Yuxuan Li − *Key Laboratory of Analytical Science for Food Safety and Biology (MOE & Fujian Province), Department of Chemistry, Fuzhou University, Fuzhou 350108, People's Republic of China*

Wei Lin − *Key Laboratory of Analytical Science for Food Safety and Biology (MOE & Fujian Province), Department of Chemistry, Fuzhou University, Fuzhou 350108, People's Republic of China;* orcid.org/0000-0002-5046-4765

Complete contact information is available at: https://pubs.acs.org/10.1021/acs.analchem.2c01373

Author Contributions

[§]R. Z. and H. G. contributed equally to this work.

Notes

The authors declare no competing financial interest.

■ ACKNOWLEDGMENTS

The authors gratefully acknowledge the financial support from the National Natural Science Foundation of China (grant nos. 21874022 and 21675029). The authors also thank Fujian Provincial Hospital (China) for providing the clinical samples for the method-comparison study.

■ REFERENCES

(1) Shu, J.; Tang, D. *Anal. Chem.* **2020**, *92*, 363−377.
(2) Zeng, R.; Huang, Z.; Wang, Y.; Tang, D. *Chemelectrochem* **2020**, *7*, 1537−1541.
(3) Zeng, R.; Luo, Z.; Su, L.; Zhang, L.; Tang, D.; Niessner, R.; Knopp, D. *Anal. Chem.* **2019**, *91*, 2447−2454.
(4) Zeng, R.; Zhang, L.; Luo, Z.; Tang, D. *Anal. Chem.* **2019**, *91*, 7835−7841.
(5) Chen, M.; Mo, F.; Meng, H.; Wang, C.; Guo, J.; Fu, Y. *Anal. Chem.* **2021**, *93*, 2464−2470.
(6) Li, F.; Wang, S.; Yin, H.; Chen, Y.; Zhou, Y.; Huang, J.; Ai, S. *ACS Sens.* **2020**, *5*, 1092−1101.
(7) Zeng, R.; Lian, K.; Su, B.; Lu, L.; Lin, J.; Tang, D.; Lin, S.; Wang, X. *Angew. Chem. Int. Ed.* **2021**, *60*, 25055−25062.
(8) Lin, Y.; Zhou, Q.; Tang, D.; Niessner, R.; Yang, H.; Knopp, D. *Anal. Chem.* **2016**, *88*, 7858−7866.
(9) Qin, Y.; Wen, J.; Zheng, L.; Yan, H.; Jiao, L.; Wang, X.; Cai, X.; Wu, Y.; Chen, G.; Chen, L.; Hu, L.; Gu, W.; Zhu, C. *Nano Lett.* **2021**, *21*, 1879−1887.
(10) Zhu, L.; Lv, Z.; Yin, Z.; Tang, D. *Anal. Chim. Acta* **2021**, *1149*, 338215.
(11) Yu, Z.; Tang, Y.; Cai, G.; Ren, R.; Tang, D. *Anal. Chem.* **2019**, *91*, 1222−1226.
(12) Zeng, R.; Luo, Z.; Zhang, L.; Tang, D. *Anal. Chem.* **2018**, *90*, 12299−12306.
(13) Zeng, R.; Tao, J.; Tang, D.; Knopp, D.; Shu, J.; Cao, X. *Nano Energy* **2020**, *71*, 104580.
(14) Alam, A. U.; Clyne, D.; Jin, H.; Hu, N.-X.; Deen, M. J. *ACS Sens.* **2020**, *5*, 412−422.
(15) Beduk, T.; Beduk, D.; de Oliveira Filho, J. I.; Zihnioglu, F.; Cicek, C.; Sertoz, R.; Arda, B.; Goksel, T.; Turhan, K.; Salama, K. N.; Timur, S. *Anal. Chem.* **2021**, *93*, 8585−8594.
(16) Guo, J. *Anal. Chem.* **2016**, *88*, 11986−11989.
(17) Huang, X.; Xu, D.; Chen, J.; Liu, J.; Li, Y.; Song, J.; Ma, X.; Guo, J. *Analyst* **2018**, *143*, 5339−5351.
(18) Roda, A.; Michelini, E.; Zangheri, M.; Di Fusco, M.; Calabria, D.; Simoni, P. *TrAC, Trends Anal. Chem.* **2016**, *79*, 317−325.
(19) Chen, J. S.; Ma, E.; Harrington, L. B.; Da Costa, M.; Tian, X.; Palefsky, J. M.; Doudna, J. A. *Science* **2018**, *360*, 436−439.
(20) Liu, J.; Wan, Q.; Zeng, R.; Tang, D. *Anal. Methods* **2021**, *13*, 3227−3232.
(21) Xiong, Y.; Zhang, J.; Yang, Z.; Mou, Q.; Ma, Y.; Xiong, Y.; Lu, Y. *J. Am. Chem. Soc.* **2020**, *142*, 207−213.
(22) Zeng, R.; Wang, W.; Chen, M.; Wan, Q.; Wang, C.; Knopp, D.; Tang, D. *Nano Energy* **2021**, *82*, 105711.
(23) Gong, H.; Wu, Y.; Zeng, R.; Zeng, Y.; Liu, X.; Tang, D. *Chem. Commun.* **2021**, *57*, 8977−8980.
(24) Li, Y.; Li, T.; Liu, B.-F.; Hu, R.; Zhu, J.; He, T.; Zhou, X.; Li, C.; Yang, Y.; Liu, M. *Chem. Commun.* **2020**, *56*, 12526−12529.
(25) Shen, Q.; Sun, L.; Zhuang, Y.; Zhan, W.; Wang, X.; Han, X. *Inorg. Chem.* **2020**, *59*, 17650−17658.
(26) Xu, H.; Wang, Y.; Dong, X.; Zheng, N.; Ma, H.; Zhang, X. *Appl. Catal., B* **2019**, *257*, 117932.
(27) Hou, J.; Cao, S.; Sun, Y.; Wu, Y.; Liang, F.; Lin, Z.; Sun, L. *Adv. Energy Mater.* **2018**, *8*, 1701114.